Milk protein-based cryogel monoliths as novel encapsulants of probiotic bacteria. Part I: Microstructural, physicochemical, and mechanical characterisation

Thierry Hellebois, Romain Canuel, Frédéric Addiego, Jean-Nicolas Audinot, Claire Gaiani, Alexander Shaplov, Christos Soukoulis

Food Hydrocolloids 140 (2023) 108641

Contents lists available at ScienceDirect

Food Hydrocolloids

journal homepage: www.elsevier.com/locate/foodhyd

Milk protein-based cryogel monoliths as novel encapsulants of probiotic bacteria. Part I: Microstructural, physicochemical, and mechanical characterisation

Thierry Hellebois [a,b], Romain Canuel [a,c], Frédéric Addiego [d], Jean-Nicolas Audinot [d], Claire Gaiani [b], Alexander S. Shaplov [d], Christos Soukoulis [a,*]

[a] Environmental Research and Innovation (ERIN) Department, Luxembourg Institute of Science and Technology (LIST), 5 avenue des Hauts-Fourneaux, Esch-sur-Alzette, L4362, Luxembourg
[b] Université de Lorraine, LIBio, F-54000, Nancy, France
[c] École Nationale Supérieure de Chimie, de Biologie et de Physique (ENSCBP), Bordeaux INP, Pessac, France
[d] Materials Research and Technology (MRT) Department, Luxembourg Institute of Science and Technology (LIST), 5 avenue des Hauts Fourneaux, L4362, Esch-sur-Alzette, Luxembourg

ARTICLE INFO

Keywords:
Whey
Sodium caseinate
Cryogel
Scaffold
Probiotic
Acid gel

ABSTRACT

The implementation of cryogels as alternative xero-carriers for embedding labile bioactive compounds including probiotic living cells is becoming more popular. In the present work, milk protein-based cryogels were developed by freeze-drying of indirectly acidified protein gels (10% wt. in sodium caseinate or whey protein isolate blended at varying mass ratios i.e., 1:0, 3:1, 1:1, 1:3 and 0:1) comprising *Lacticaseibacillus rhamnosus* GG (LGG) living cells, trehalose (5% wt.), glucose (1% wt.) and glycerol (2.5% wt.). The physicochemical, microstructural, and mechanical characteristics of the cryogels conveying LGG were measured. The acid gel contraction during the fermentation notably influenced the macroscopic (volume contraction) and microscopic aspects (porosity, thickness, and uniformity of the wall material construct) of the cryogels. The amount of monolayer water content (11.5–14.0 g.100 g^{-1}), and total surface area (403–488 m^2 g^{-1}) as well as the glass transition temperature (T_g = 33–46 °C), of the cryogels increased proportionally to the whey protein content. X-ray microtomography analysis revealed that the mixed protein cryogels were characterised by lower porosities than their individual protein exemplars. However, the uniformity and the structure conformation of the protein network constructs were altered according to the milk protein composition of the cryogels. All the cryogels exhibited a brittle and plastic behaviour when subjected to indentation forces, with the hardest and stiffest cryogels exerting the lowest water reconstituting capacity. The microstructural assessment of the wall material at nanoscale level evidenced a satisfactory intrenching of the LGG cells, which substantiates the feasibility of the cryogels as novel probiotic xero-scaffolds.

1. Introduction

Probiotics are defined as human gut relevant commensals and microbes that have generic or core effects on gut physiology and homeostasis or that support the health of the reproductive tract, oral cavity, lungs, skin and gut-brain axis (Hill et al., 2014). Probiotics encapsulation i.e., the physical engrafting of living cells in a structurally and/or interfacially engineered colloidal micro- or nano-template, is a very efficient technological approach to minimise the loss of the inherent biological activity of probiotics (Gu et al., 2022; Kiepś & Dembczyński, 2022; Yao et al., 2020). To date, anhydrobiotic technology i.e., xero-carriers conveying living cells usually produced via lyophilisation or spray drying, is considered the commonest strategy for probiotic encapsulation (Aschenbrenner et al., 2015; Burgain et al., 2015). Despite high operational costs and challenging upscalability, the encapsulation of probiotics in freeze-dried scaffolds allows the maximal preservation of the cells, as well as high technological versatility (Koh et al., 2022). A consolidated encapsulation system should provide satisfactory protection against several physicochemical and biological stressors encountered during processing, storage and gastrointestinal transit, such as

* Corresponding author.
E-mail address: christos.soukoulis@list.lu (C. Soukoulis).

https://doi.org/10.1016/j.foodhyd.2023.108641
Received 20 October 2022; Received in revised form 17 February 2023; Accepted 27 February 2023
Available online 28 February 2023

heat, pH, water vapour, oxygen, osmotic stress, mechanical injuries, bile salts and digestive enzymes (Capozzi et al., 2016; Gu et al., 2022; Yao et al., 2020).

Cryostructuration is an alternative biosynthetic approach for the construction of xero-scaffolds, which is based on: a) the cryogenic processing of a polymeric solution or colloidal dispersion, and b) the removal of the ice via sublimation (Lozinsky, 2018). Macromolecules such as polysaccharides and proteins have been used successfully in the fabrication of cryogels (Bektas et al., 2021; Betz et al., 2012; Groult et al., 2021; Manzocco et al., 2022; Zou & Budtova, 2021, 2021, 2021). Food biopolymer-based cryogels are recognised for their tailorable microstructural features, satisfactory mechanical durability and resilience, high biocompatibility and biodegradability, among others (Manzocco et al., 2021). Adhering to the same principles as cryostructuration, the microstructural, physicochemical, and mechanical aspects of cryogels are influenced by several parameters including the type and the concentration of biopolymeric precursors, the colloidal state of the precursor medium, and the cryogenic processing conditions (Lozinsky, 2020).

Like their mesoporous or microporous counterparts (known as aerogels), the assiduous design of the cryogenic processing is inextricably associated with the behaviour of the biopolymer precursor medium under sub-eutectic point conditions and therefore, it influences the final physicochemical and microstructural aspects (Gun'ko et al., 2013; Shiekh et al., 2021). In addition, the proper design of the cryogel precursor medium (e.g., concentration, pH, type of polymer, degree of cross-linkage etc.) is essential for preventing the risk of structural collapse (e.g., shrinkage, cracking, fissuring etc.) during the freeze-drying process (Betz et al., 2012; Chen et al., 2013; Kleemann et al., 2018). Hitherto, several food biopolymers such as polysaccharides (e.g., starch, galactomannans, alginates, carrageenans, pectins, glucans etc.) and proteins (e.g., whey proteins, caseins, albumin, gelatine etc.) have been deployed individually or as co-polymers in the development of cryogels (Fontes-Candia et al., 2022; Kleemann et al., 2018, 2020; Manzocco et al., 2021; Volkova & Berillo, 2021). In contrast with polysaccharides, the development of protein-based cryogels requires their pre-gelation induced via heating, acidification, enzymatic (e.g., rennet, transglutaminase etc.) or cryogenic (freeze-thaw) processing at concentrations close or well above their critical gelation points, which allows the formation of self-standing hydrogels. (Heidebach et al., 2009; Hellebois, Gaiani, Cambier, et al., 2022; Hellebois, Gaiani, & Soukoulis, 2022; Kleemann et al., 2020; Schorsch et al., 2000; Selmer et al., 2019).

Recent studies have showcased the feasibility of protein-based cryogels to be deployed as templates for the encapsulation of labile bioactive compounds (Ahmadi et al., 2016; Fontes-Candia et al., 2022; Kleemann et al., 2020; Manzocco et al., 2021). Stemming from their high interfacial activity, protein-based cryogels and aerogels permit satisfactory drug loading yields and encapsulation efficiency (Ahmadi et al., 2016; Kleemann et al., 2020; Manzocco et al., 2022). Protein cryogels are also appealing due to their programmable swelling and release behaviour under simulated in vitro gastrointestinal conditions (Fontes-Candia et al., 2022; Kleemann et al., 2020). Swelling trials have evidenced the constrained ability of protein aerogels to undergo disintegration in gastrointestinal fluid media, whilst their resistance to peptic cleavage is strictly dependent on the chemical structure and conformation of the protein (Fontes-Candia et al., 2022; Kleemann et al., 2020). Despite their promising techno-functional properties, there are currently no studies showcasing the suitability of cryogels in the domain of anhydrobiotics.

The aim of the present work was to study the feasibility of milk protein (whey protein and sodium caseinate)-based cryogels as alternative biopolymer scaffolds for embedding living probiotic bacteria (i.e., *Lacticaseibacillus rhamnosus* GG, LGG) cells. Part I investigates the impact of the NaCN to WPI ratios on the macroscopical appearance, microstructural conformation, chemical structure, thermo-physical, and mechanical properties of probiotic cryogel monoliths. Part II aims to explore the ability of the cryogels to preserve the biological activity of LGG throughout freeze-drying, storage and simulated in vitro digestion. In addition, the interplay between the in vitro digestion performance (colloidal changes, proteomic profile, and bacteria cell sub-lethality) and storage stability of the probiotic cryogels and their structural and physicochemical characteristics will be elucidated.

2. Materials and methods

2.1. Materials

Whey protein isolate powder (PRODIET 90S) with a protein content of 85.8% wt. was kindly donated by Ingredia (Arras, France). Sodium caseinate (containing 89.4% wt. of protein), glucose (99.5% wt.) and glycerol (99.9% wt.) were purchased from Sigma-Aldrich (Leuven, Belgium). Trehalose dihydrate (99.4% wt.) was purchased from Louis-François (Croissy-Beaubourg, France). The probiotic strain LGG (ATCC 53103) used was purchased from the VTT Technical Research Centre of Finland Ltd (Espoo, Finland). All other chemicals were analytical grades.

2.2. Preparation of the hydrogels and cryogels

The appropriate amount of whey protein isolate (WPI) or sodium caseinate (NaCN) was dispersed in Milli-Q to obtain a final protein dispersion of 10% wt. The protein dispersions were kept under magnetic stirring at ambient temperature overnight (IKA GmbH, Staufen, Germany) to allow sufficient hydration and were three-times homogenised at 500 bar (Panda plus 2000, Gea GmbH, Germany) to break down any protein agglomerates. Then, the milk protein solutions were centrifuged at 10000*g* for 5 min to remove any insoluble residual. The absence of protein agglomerates was confirmed by static laser light scattering particle size analysis (Mastersizer 3000, Malvern Instruments, Worcestershire, UK). The amount of protein content was verified by the Dumas method using an organic elemental analyser (Vario Cube, Elementar GmbH, Langenselbold, Germany). Then, trehalose, glycerol, and glucose were added to the solution to obtain a final concentration of 5, 2.5 and 1% wt., respectively. The NaCN and WPI solutions were then mixed to obtain five different NaCN:WPI mass ratios ($m_{NaCN/WPI}$) as follows: 1:0, 3:1, 1:1, 1:3 and 0:1. The final protein solutions were heat-treated at 80 $\pm$ 1 °C for 20 min in a shaking water bath (SW22, Julabo, Seelbach, Germany) before being rapidly cooled in an ice bath.

A pre-culture of LGG was prepared by growing aliquots from the cryovials (Microbank 2D, Novolab, Geraardsbergen, Belgium) overnight in a MRS broth under anaerobic conditions at 37 $\pm$ 1 °C. The next day, the LGG culture was prepared by seeding 100 μL of the pre-culture in 50 mL of fresh MRS broth. At the end of the exponential phase (approximatively 14 h), the bacteria cell suspension was centrifuged (7000*g*, 2 min) and washed twice with a phosphate-buffered saline (PBS) solution.

To induce the lactic-acid gelation of the milk protein solutions, 4 LGG cell pellets were dispersed within a protein solution of 100 mL. Then, aliquots (1 mL) of the inoculated solutions were rapidly transferred in 24-well plates (Corning, Corning, NY, United States) and incubated for 4 h at 37 $\pm$ 1 °C. On completion of the gelation, the samples were frozen at −80 °C for 2 h and underwent a two-stage freeze-drying (18 h at 0.120 mbar followed by 22 h at 0.010 mbar). The resulting cylindrical cryogels (diameter $\times$ height = 15 $\times$ 10 mm) were stored in hermetically sealed containers filled with P_2O_5 to prevent water absorption until further use.

2.3. Monitoring of gelation and characterisation of the acid-induced gels

2.3.1. Dynamic rheological measurements

Dynamic rheological measurements were performed in duplicate with an oscillatory rheometer (MCR 302, Anton Paar, Graz, Austria) using a double gap system (DG 26.7) of diameter 27.1 mm. Eight mL of the LGG-inoculated protein solution were transferred to the measuring cell and covered with a thin layer of silicone oil to prevent water

evaporation. The temperature was then raised to 37 ± 0.05 °C to promote the fermentation and the gelation *in-situ*. The viscoelastic properties of the systems were measured every 30 s for 4 h at constant shear strain (0.1%) and frequency (1 Hz). In addition, the pH of the systems was recorded using a multi-3430 pH-meter (WTW, Weilheim in Oberbayern, Germany).

2.3.2. Acid-induced gel stability

The gel colloidal instability due to the spontaneously occurring syneresis was assessed in four independent fermented gels using a LUMiSizer (LUM GmbH, Berlin, Germany). The protein solutions were fermented for 4 h at 37 ± 1 °C in 10 mm polycarbonate LUM cells. The resistance of the final hydrogels to forced serum exudation was assessed by monitoring the light transmittance (λ = 865 nm) over the tube height at 2300*g* for 10 min with a 5 s interval between measurements at 25 °C. Data analysis was performed using the SEPView software (LUM GmbH, Berlin, Germany).

2.3.3. Confocal laser scanning microscopy (CLSM)

The microstructural features of the fresh hydrogels (i.e., after 4 h of incubation at 37 °C) were visualised using a CLSM microscope (LSM 880 with Airy scan, Zeiss, Jena, Germany). Freshly inoculated protein solutions were transferred into 1 mL Eppendorf containing 10 μL of protein staining reagent (Fast Green, λ_{Ex} = 633 nm, λ_{Em} = 635–680 nm), 1.5 μL of stain for living (SYTO9, λ_{Ex} = 488 nm, λ_{Em} = 498–550 nm) and 1.5 μL of stain for dead (propidium iodide, λ_{Ex} = 488 nm, λ_{Em} = 585–640 nm) bacteria (LIVE/DEAD BacLight, Thermo Fisher Scientific, Waltham, MA, United States). The samples were homogenised using a benchtop vortex and 300 μL were transferred into eight-chambered microscope slides (Nunc Lab-Tek II, Thermo Fisher Scientific, Waltham, MA, United States). The microstructural assessment was performed using a × 40 objective.

2.4. Characterisation of the cryogels

2.4.1. Thermophysical properties

The thermal behaviour of the freshly produced cryogels was assessed in duplicate by differential scanning calorimetry (DSC), thermogravimetric analysis (TGA), and thermo-mechanical analysis (TMA). The DSC analysis was performed on an SC3+ System (Mettler Toledo, Zurich, Switzerland) implementing a heating-cooling protocol as follows: 1) heating from −30 to 150 °C, 2) isothermal hold at 150 °C for 5 min, 3) cooling from 150 to −30 °C, and 4) heating from −30 to 150 °C. All the heating/cooling ramps were performed at a constant rate of 10 °C.min^{-1}. The midpoint glass transition (T_g) was calculated as the bisector of the angle between the tangents of the curve above and below the glass transition event.

The TGA was carried out in an air atmosphere using a TGA2 STARe System (Mettler Toledo, Zurich, Switzerland), applying a heating rate of 5 °C.min^{-1} from 25 to 600 °C. The onset weight loss temperature (T_{onset}) was determined as the point in the TGA curve at which a significant deviation from the horizontal was observed. The midpoints of the mass loss rate changes were determined as the peaks of the first derivative curves (DTG). Finally, the samples underwent TMA under inert atmosphere (He) using a DIL 402 select Expedis dilatometer (Netzsch, Germany) at a heating rate of 10 °C.min^{-1} and a constant load of 0.3 N in the temperature range from −80 to 150 °C. In addition, all the individual components of the cryogels were analysed using TMA and TGA.

2.4.2. Mechanical properties of the cryogels

The mechanical collapse of the cryogels was measured using an 8 mm plate-plate probe mounted on an oscillatory rheometer (MCR 302, Anton Paar, Graz, Austria). The cryogels (approx. 400 mg) were desiccated in P_2O_5 for 3 weeks until moisture equilibrium was reached.

For the mechanical testing, the desiccated sample was placed sideways on a sand-blasted 25 mm plate geometry and the penetration depth and speed were set at 10 mm and 1 mm s^{-1}, respectively. The normal force (N)-penetration depth curves of at least 12 individual samples were analysed using Origin 2019b software (OriginLab Inc, Northampton, MA, United States) and the following parameters were calculated: a) hardness (in N, normal force maximum) b) stiffness (in N.mm^{-1}, the slope of the curve) and the work required to break the cryogel (in mJ, area under the peak until break). An example of peak analysis is shown in Suppl. Fig. 1.

2.4.3. Protein secondary structure

Two different aliquots of the cryogels were ground with KBr (at a 1:100 wt ratio) and compression-moulded into a pellet. Fourier-Transform Infrared spectroscopy (FTIR) spectra were recorded in the range of 4000–500 cm^{-1} using an Optics Vertex spectrometer (Bruker, Billerica, MA, United States) with the Attenuated Total Reflectance (ATR) mode and a resolution of 2 cm^{-1}. The ATR crystal is a diamond with an active sampling area of 0.8 mm in diameter and a reflection angle of 45°. Spectra were obtained from 50 scans. The baseline spectra were calculated without samples and subtracted from the obtained cryogel spectra. The deconvolution of the amide I region (i.e. 1700–1600 cm^{-1}), corresponding to C=O stretching, was conducted using Origin 2019b software (Jackson & Mantsch, 1995).

2.4.4. Hygroscopicity

The water vapour sorption dynamics of the cryogels (water activity, a_W 0–0.85) from two independent experiments were determined using a dynamic vapour sorption analyser (DVS, Surface Measurement Systems Ltd., London, United Kingdom). A sample of approx. 80 mg was placed into the sealed chamber and dried under a water-free atmosphere until the mass reached an equilibrium (20 ± 0.1 °C). The relative humidity of the chamber was increased stepwise i.e., a_W = 0, 0.11, 0.23, 0.33, 0.44, 0.54, 0.64, 0.75, 0.80 and 0.85, and the respective water mass uptake at the equilibrium was recorded. The points obtained were fitted with the Guggenheim-Anderson-De Boer (GAB, Eq. (1), a_W = 0−0.85) (van den Berg & Bruin, 1981) models using the Origin 2019b software. To this end, the following equation was considered:

$$X = \frac{X_m C k a_w}{(1 - k a_w)(1 - k a_w + C k a_w)} \quad (1)$$

where X denotes the moisture at the equilibrium, X_m the moisture content at the monolayer, C, is a constant that depicts the free enthalpy energy difference between the monolayer and pure liquid water molecules, k is the constant correcting the properties of the multilayer molecules, and a_w the water activity. From Eq. (1), the total surface of the monolayer S_m, can be obtained as follows (Eq. (2)):

$$S_m = X_m \frac{1}{M_{H_2O}} N_A A_{H_2O} = 3.5 \times 10^3 X_m \quad (2)$$

where X_m is analogous with the GAB equation, M_{H_2O} is the molecular weight of water (18 g mol^{-1}), A_{H_2O} is the area of a single water molecule (1.06×10^{-19} m^2), and N_A is the Avogadro number (6×10^{23} molecules.mol^{-1}) (Mazza & LeMaguer, 1978).

2.4.5. Assessment of the morphological aspects

2.4.5.1. Degree of shrinkage. The ability of cryogels to retain the dimensional characteristics of the precursor hydrogel system was assessed volumetrically according to equation (3):

$$\text{Shrinkage } (\%) = 100 \frac{V_p - V_c}{V_p} \quad (3)$$

where V_p and V_c denote the volume (in cm^3) of the initial precursor aliquot (prior to fermentation) and the freeze-dried cryogel obtained. The volume of pre-weighted cryogel monoliths was calculated using a

silica beads (mean particle size 40 − 75 μm) displacement method. The bulk density (ρ, in $g.cm^{-3}$) was then calculated as $\rho = m_c/V_c$, where m_c and V_c are the masse and volume of the cryogels, respectively. The density was expressed as the mean value of eight cryogels.

2.4.5.2. X-ray tomography. Micro-computed X-ray tomography (μCT) measurements were performed to visualise and quantify the 3D microstructure of the desiccated cryogels in duplicate. To this end, a laboratory X-ray cone-beam μCT system EasyTom 160 from RX Solutions (Chavanod, France) was used at 60 kV and 120 μA. 1440 projections over 360° (step of 0.25°) were recorded at 0.5 frames s^{-1} by a 16-bit flat panel imager with a total pixel area of 1920 pixels × 1536 pixels. The source-to-object distance (SOD) and the source-to-detector distance (SDD) were set to approx. 2.2 mm and 320 mm, respectively, enabling us to obtain a voxel size of approx. 0.9 μm. Xact software (RX Solutions, Chavanod, France) was used with the projections acquired to reconstruct the volume into stacked slices after applying a sample movement correction (spot deviation module), a system misalignment correction (geometry correction module) and a ring filter (5 pixels). The slices were subsequently analysed by means of the 3D image analysis software Avizo (Konrad-Zuse-Zentrum Berlin/FEI SAS-Thermo Fisher Scientific, Waltham, MA, United States). The following procedure was applied: median filter (3D mode, 6 neighbourhoods) to facilitate the segmentation, grey-level segmentation to isolate the pores and the matrix, quantification of the pore volume fraction and, thickness map analysis of the matrix (vessel thickness distribution).

2.4.5.3. Scanning electron microscopy (SEM) and helium ion microscopy (HIM). The microstructural aspects of the macroporous protein network were assessed using a field emission scanning electron microscope (SEM, SU-70, Hitachi, Tokyo, Japan). The cryogels were fractured and fixed on aluminium stubs using a carbon tape, coated with 5 nm of platinum (ACE 600, Leica microsystems, Wetzlar, Germany) and analysed using an acceleration of 5 kV, a working distance of 15 mm and a magnification of × 350.

To gain insight into the encapsulation efficiency of the cryogels and the microstructural conformation of the vessels, a Zeiss Orion NanoFab Helium Ion Microscope (HIM, Zeiss Microscopy, Peabody, MA, United States) with the secondary electron detection mode using an Everhardt−Thornley detector was employed. To benefit from the high lateral resolution of the HIM, the primary source was a Helium beam generated in the Gas Field Ion Source, with an acceleration of 25 keV and a current of 0.3 pA. The images were acquired in 1024 pixels × 1024 pixels, with a counting time of 10 μs per pixel and an average of 4 lines. Samples were coated with a thin gold film (5 nm) to prevent a charge effect.

2.4.6. Disintegration profile of the cryogels

The disintegration profile of the cryogels was carried out using static light scattering (Mastersizer 3000, Malvern Instruments, Worcestershire, United Kingdom). The experiment was run by immersing a cryogel in the LV measuring cell filled with Milli-Q water under constant stirring at 3500 rpm for 15 min at 25 ± 1 °C. The particle size distribution was recorded with interval of 10 s during 3 s with blue and red lasers. The refractive index was set at 1.45. The data was then fitted with a first order exponential model (Eq. (4)) as follows:

$$y = D_{[4,3]_\infty} + \left(D_{[4,3]_0} - D_{[4,3]_\infty}\right) e^{-\frac{\ln 2 \cdot t}{\tau_{1/2}}} \quad (4)$$

where $D_{[4,3]_0}$ and $D_{[4,3]_\infty}$ denote the volume-weighted mean particle size (μm) at t = 0 and ∞ min, t the time (s) and $\tau_{1/2}$ the time required to reach a 50% $D_{[4,3]_0}$ decrease (Quodbach & Kleinebudde, 2014).

2.5. Statistical analyses

The Shapiro-Wilk test and Q–Q plot representation normality tests were used to verify the normal distribution of the data. To determine the significant differences, one-way ANOVA was performed using Origin 2019b software (OriginLab Inc, United States). The Tukey's multiple range test was used to separate mean values when significant differences ($p < 0.05$) were detected. All results were expressed as mean ± standard deviation.

3. Results and discussion

The microstructure conformation and consequently, the physicochemical and mechanical properties of cryogels are influenced by several parameters, including the type and concentration of the polymeric precursors, the presence of kosmotropic small molecules (e.g., sugars) and the cryogenic processing conditions (Lozinsky, 2020). Previous studies have shown that the bestowed physicochemical, structural, and mechanical characteristics of cryogels are inextricably associated with the microstructure and physical state of their hydrogel precursor(s) (Betz et al., 2012; Kleemann et al., 2018; Selmer et al., 2015). In this context, the microstructural, dynamic rheological properties and colloidal stability of the acid-induced hydrogel precursors were studied first.

3.1. Characterisation of the acid-induced hydrogels

The indirect acid-induced gelation curves, as influenced by the protein composition, are illustrated in Fig. 1. As expected, the onset gelation point increased exponentially (R^2 = 0.999) to $m_{NaCN/WPI}$ ranging from $t_{gel,\ onset}$ = 27–170 min. The differences in the gelation kinetics were ascribed primarily to the higher isoelectric point of WPI (~5.2) and the ability of the non-sedimentable whey protein aggregates (ca. 240 nm as determined in this study by DLS analysis) to interact via hydrophobic and hydrogen bridging interactions at the very early stage of gelation i.e., at a pH far from the pI (Donato et al., 2011). As NaCN becomes more prevalent in the milk protein mixture, the intermolecular bridging of the WPI fractals is sterically hindered due to the competing action of NaCN for Ca^{2+}, leading to the slowdown of the gel formation (Nguyen et al., 2016). According to the dynamic rheological spectra, the individual protein gels showed minimal colloidal rearrangements

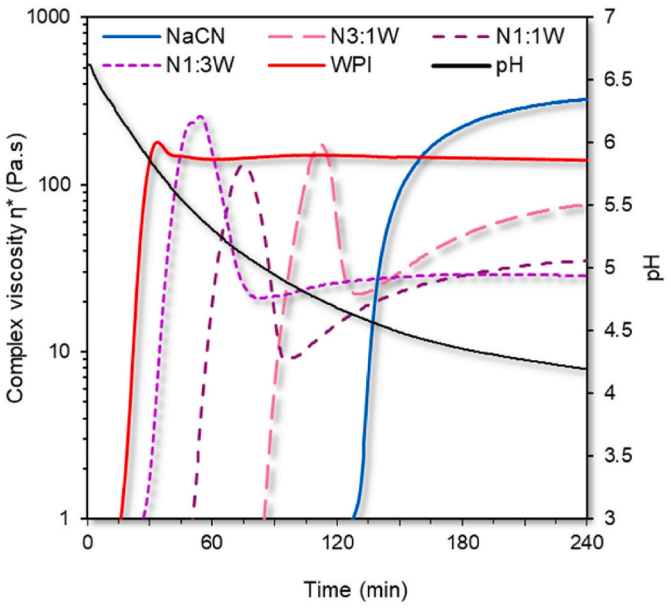

Fig. 1. Representative lactic acid-induced protein gelation profiles of the NaCN and WPI, as well as their blends determined by isothermal oscillatory rheology (f = 1 Hz, γ = 0.1%, 37 °C). The decline of pH throughout the fermentation is represented by the continuous black line.

throughout gelation, as depicted by the absence of an abrupt decrease in the complex viscosities after the gelation inflection (t_θ) time point (Fig. 1). In the case of NaCN-WPI mixtures, an approximative one-order reduction in the η^* values was observed at $t \sim t_\theta$, a phenomenon that is most probably associated with the molecular interaction between the WPI fractals and NaCN via covalent thiol-disulphide bonding. In succession, the re-organised protein gel networks commenced slowly restoring their mechanical properties due to the stabilisation of the protein network via supramolecular interactions i.e., hydrogen bonding between the heteroprotein aggregate clusters (Lucey, 2020). Nonetheless, the assiduous investigation of the gelation mechanisms was out of the scope of the present study.

In Fig. 2, the stability of the gel was assessed when faced with spontaneous serum exudation from the protein gel network. Both NaCN and WPI hydrogels showed insignificant changes in the light transmission measured across the tube height reflecting negligible serum exudation (Fig. 2A,E,F). Contrarily in the NaCN-WPI blends (Fig. 2B–D, F), a significant increase in the instability index values ($p < 0.001$) was observed. Interestingly, the colloidal stability of the acid-induced gels was positively correlated with change in the complex viscosity $\Delta\eta^*$ at $t \sim t_\theta$ ($r = 0.777$, $p < 0.01$), implying that the microstructural re-organisation occurring in the binary protein gel systems hampered their capacity to prevent the serum from outflowing through the porous protein network (Lucey, 2002).

From a microstructural point of view (Fig. 3), WPI resulted in the formation of homogenous fine-stranded gels (Fig. 3, A5) whilst NaCN exhibited a well-defined aggregated-like microstructure (Fig. 3, A1). This behaviour is consistent with the results from the literature (Pugnaloni et al., 2005; Soukoulis et al., 2019). In the case of NaCN-WPI hydrogels, composite protein gel networks combining, in a proportional manner, the microstructural features of the individual proteins were detected (Figs. 3, 2–4). According to the acquired CLSM micrographs, only the LGG cells located in the voids of the protein network could be clearly identified, without any evidence of acute lethality (as indicated by the presence of red stained bacterial cells) occurring during the fermentation step (Fig. 3, B1-5). Finally, the WPI-rich hydrogels enhanced the embedding of the LGG cells in a continuous protein network compared to their NaCN-rich counterparts, which may be associated with the better cell adhesion capacity of the former (Gomand et al., 2019).

3.2. Characterisation of the cryogels

It is well-accepted that glassy and non-hygroscopic carriers that are less permeable to gases (water vapour and oxygen) are generally associated with the enhanced stability of probiotic cells during storage (Aschenbrenner et al., 2015). In addition, the microstructural conformation and the mechanical profile of the embedding carrier may play a significant role in controlling its disintegration and tuning the bacterial cell release behaviour, preserving the biological role of probiotics throughout gastrointestinal transit (Jiang et al., 2022). In view of this, the physicochemical, microstructural, mechanical and matrix disintegration aspects of the cryogels were determined.

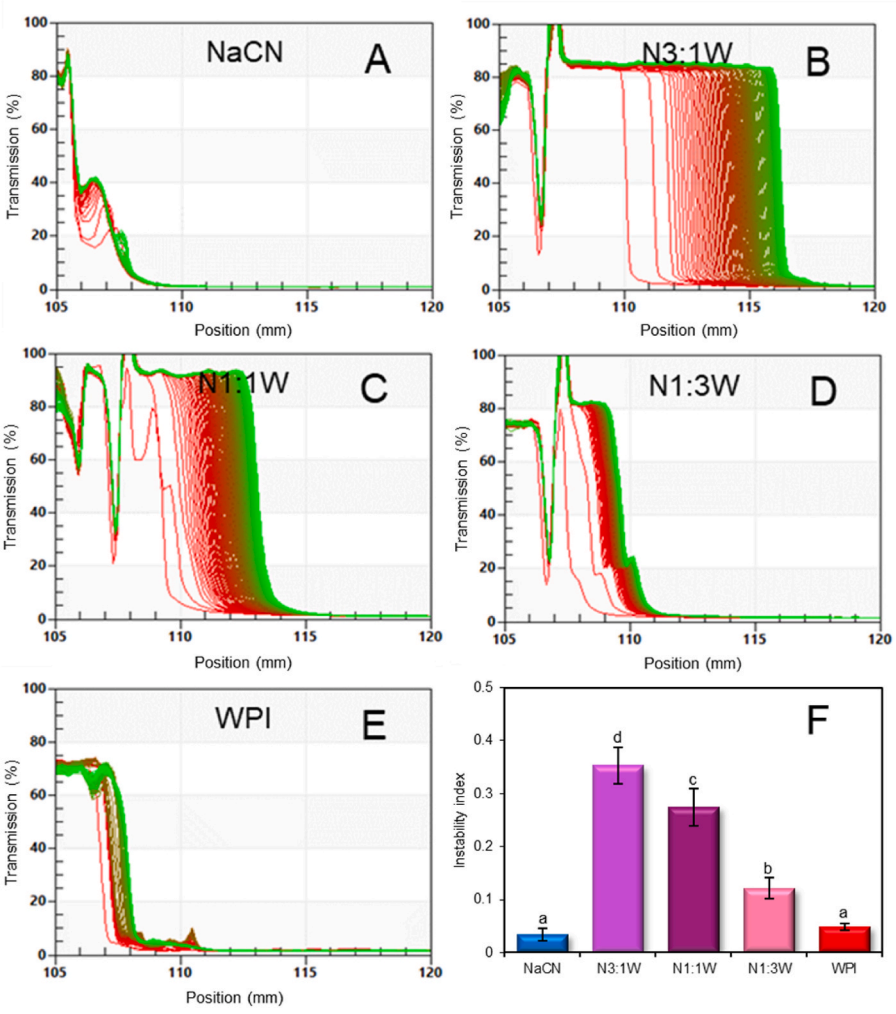

Fig. 2. Dynamic light transmission spectra of NaCN, WPI hydrogels and their blends (A–E) for assessing the temporal evolution of the colloidal stability under accelerated storage conditions (25 °C, 2300*g*). Their respective instability indexes (dimensionless) are depicted in F. Red lines and green lines represent the first and last scanning, respectively. $^{a\text{-}d}$Different letters between the cryogels (F) denote a significant difference ($p < 0.05$) according to Tukey's post hoc means comparison test. Error bars = standard deviation ($n = 4$).

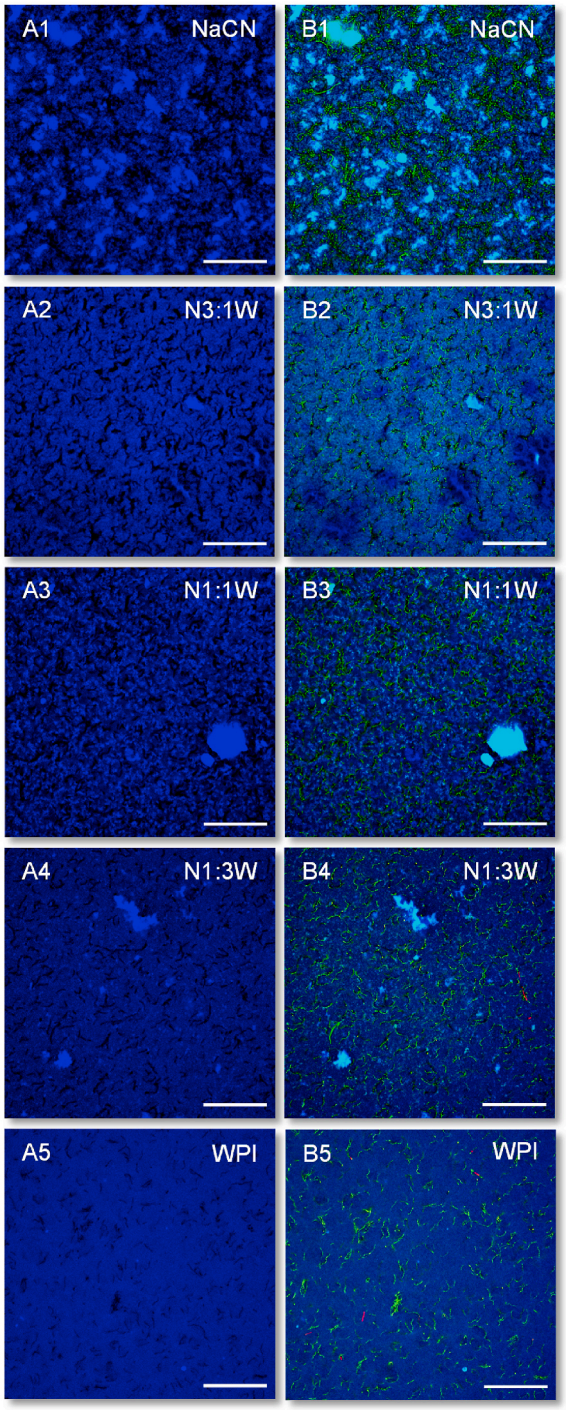

Fig. 3. CLSM micrograph of NaCN, WPI and mixture acid-gels obtained after 4 h of fermentation (37 °C). The protein network (in blue) was stained using Fast Green (λ_{Ex} = 633 nm, λ_{Em} = 635–680 nm) while living (in green) and dead (in red) LGG cells were stained with SYTO9 and propidium iodide, respectively. All the samples were analysed with a 40 × objective. For improved readability, the microstructure of the protein network is displayed with a single channel staining (A) whereas the LGG distribution is highlighted with green and red staining (B). Scale bar = 50 μm.

3.2.1. *Macroscopic appearance and microstructural characteristics*

From a macroscopic viewpoint, the single protein-based cryogels preserved the geometrical (shape and size) aspects of their hydrogel precursors satisfactorily (Fig. 4A,E). However, the mixed protein cryogels underwent volume contraction (Fig. 4B,C,D, Fig. 5) and shape

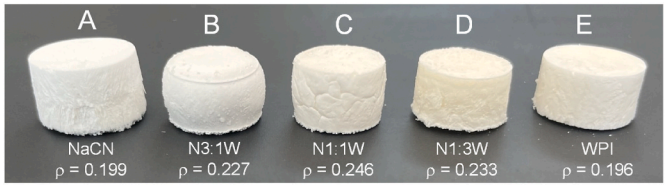

Fig. 4. Macroscopic appearance of the milk protein cryogel monoliths embedding LGG cells. The bulk density of the cryogels (ρ, n = 8) is expressed in g.cm^{-3}. Approximative cryogel dimensions: diameter × height = 15 × 10 mm.

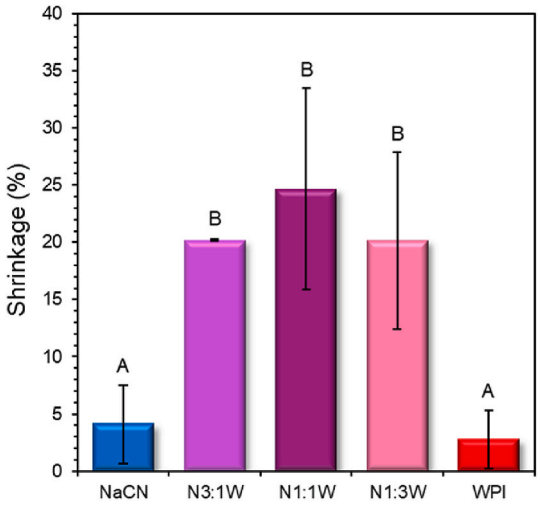

Fig. 5. Degree of shrinkage of the milk protein cryogel monoliths compared to the initial volume of solution. $^{A-B}$Different letters between the cryogels denote a significant difference ($p < 0.05$) according to Tukey's post hoc means comparison test. Error bars = standard deviation (n = 8).

distortion (Fig. 4B). A good correlation was found between the cryogel shrinkage percentage and the precursor hydrogel colloidal instability index, which implies that the extent of the contraction of the protein gels during the acidification process defines the macroscopical properties of the cryogels and therefore, the optimisation of the fermentation process parameters e.g., inoculum size, temperature, use of symbiotic cultures, presence of other hydrocolloids, enzymatic crosslinking, etc. (Soukoulis et al., 2007) needs to be thoroughly considered in the cryostructuration of indirectly acid-induced cryogels. In addition, the increase in total milk protein solids (at $c > c_{Least\ Gelation}$) may assist to retain the shape and size characteristics of precursor hydrogels, but the inclusion of the living probiotic cells would become challenging, particularly if the impregnation method is implemented as in the case of other bioactives (Betz et al., 2012; Selmer et al., 2015, 2019).

To evaluate the impact of the fermentation step on the microstructural characteristics (e.g., microporosity and microstructure of the wall material), the probiotic cryogels were analysed by μCT (Fig. 6A–C), SEM (Fig. 6D) and HIM (Fig. 6E). On one hand, as illustrated in μCT volume renderings, the single protein cryogels had the most porous structure, indicated by the macropore volume fraction measured, i.e., $\varphi = 0.78$. On the other hand, the mixed protein hydrogels were significantly ($p < 0.001$) less porous $\varphi = 0.67-0.72$, which is attributed to the compacted microstructure of their acid-induced hydrogel precursors. In agreement with the μCT images, SEM analysis confirmed that the single protein and N1:3W-based cryogels (Fig. 6 D1,4–5) were characterised by a honeycomb-like microstructure, with the smallest macropores size observed in the NaCN-based cryogels. On the other hand, the single protein-based cryogels exerted a fairly rough vessel surface compared to the N1:3W. In the latter case, a high degree of lacunarity and the presence of a crystalline-like structure with sharp edges was detected.

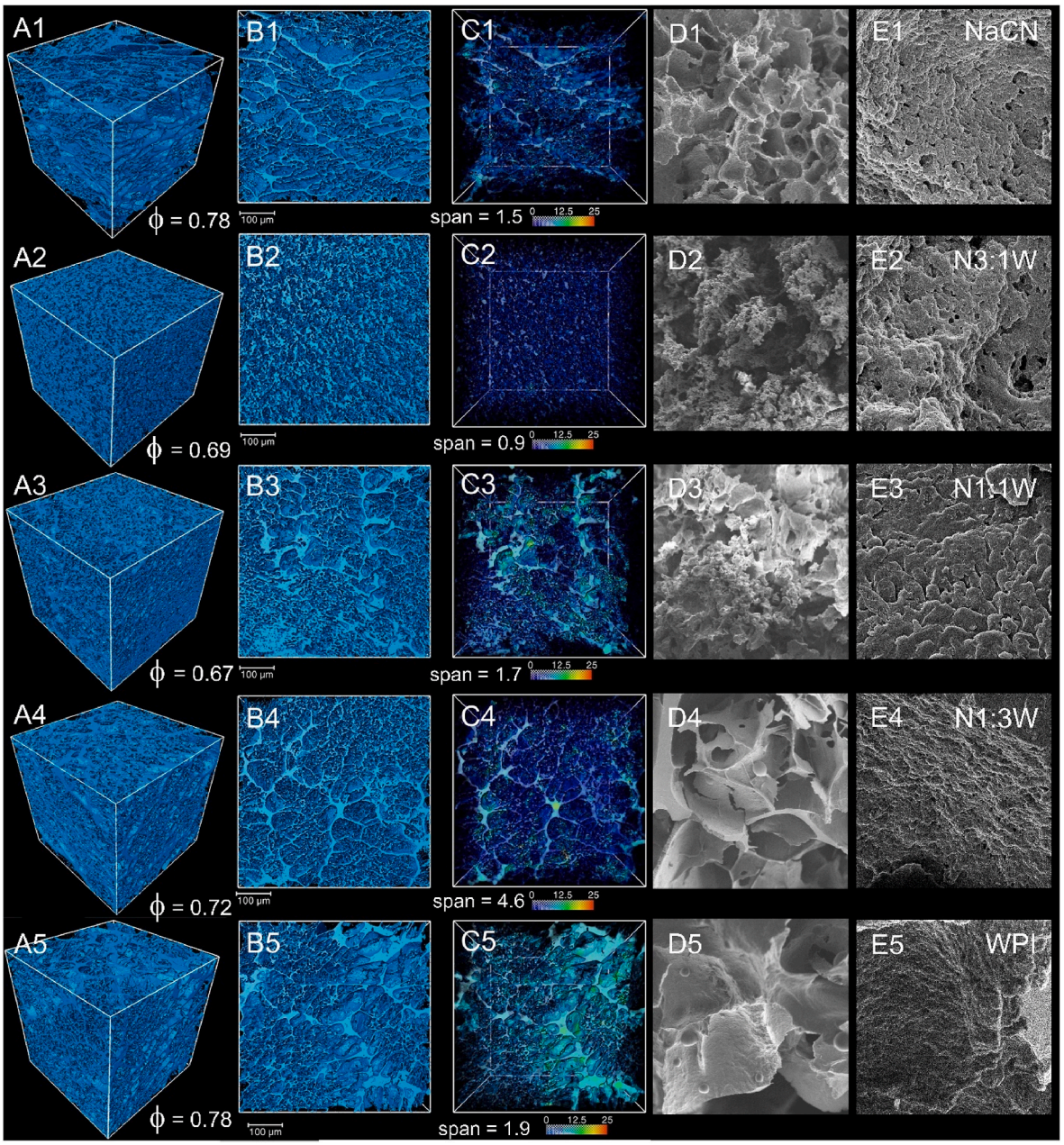

Fig. 6. µCT volume rendering with an angular view (A1–5), front view (B1–5) and front view after vessel thickness analysis (range 0–25 µm, C1–5), SEM (D1–5) and HIM (E1–5) micrographs in the case of NaCN (1), NaCN:WPI blends (2, 3 and 4) and WPI (5) cryogels. Dimensions of: µCT volume rendering = 500 × 500 × 500 voxels (voxel size of about 0.9 µm), SEM micrographs = 240 × 240 µm^2, and HIM micrographs = 8 × 8 µm^2. Abbreviations used: φ: porosity volume fraction; span: cryogel vessel thickness uniformity defined as vt_{90}-vt_{10}/vt_{50}. (n = 2). High resolution SEM images can be found in the supplementary material (Suppl. Fig. 2).

Finally, the N3:1W and N1:1W (Fig. 6 D1−2) samples portrayed a relatively compact structure consisting of globular agglomerated sub-units, with the N3:1W former exerting the highest structure-conformational uniformity.

To gain a better insight into the uniformity of the interconnected: vessel network of the cryogels, the cumulative vessel thickness curves were constructed, and a three-parameter sigmoidal model (Eq. (5)) was fitted as follows:

$$y = 100\frac{a}{1+\left(\frac{x}{b}\right)^n} \quad (5)$$

where: a is an asymptomatic value (100%), b denotes the inflection point that represents the area at 50% of the cumulative distribution function, and n is a constant associated with the rate of change (slope) of the distribution. In general, the median vessel thickness (vt_{50}) ranged from 2.9 to 3.9 µm without showing a clear dependence on the protein composition of the cryogels. However, the vessel thickness distribution width values (i.e., span = vt_{90}-vt_{10}/vt_{50}) increased in this cryogel order: N3:1W < NaCN < N1:1W – WPI < N1:3W, which indicates that a proper consideration of the protein precursor composition is required in order to achieve a fine and uniform filamentous cryogel construct.

HIM analysis was carried out to provide insight into the submicron structure of the cryogel monoliths wall material (Fig. 6E) as a qualitative assessment of encapsulation efficiency. To a large extent, a satisfactory intrenching of the cells of LGG into the continuous protein networks was observed, which substantiates the feasibility of cryogels as alternative xero-carriers for embedding living probiotic cells (Suppl. Fig. 3). In regard to the impact of the $m_{NaCN/WPI}$ on the wall material microstructure

(Fig. 6E), the prevalence of NaCN was associated with a quite coarse microstructure composed of densely packed layers of scale-like, reticular conformations, which is in agreement with the observations of (Soukoulis et al., 2016). In contrast, the WPI-rich cryogels were characterised by a more compact and less perforated microstructure of globular-like protein aggregate conformations (Manzocco et al., 2022; Selmer et al., 2019; Soukoulis et al., 2017).

3.2.2. Protein secondary structure conformation

The FTIR spectra of the probiotic cryogels influenced by the $m_{NaCN/WPI}$ are illustrated in Fig. 7A. As expected, the amide I, 1700–1600 cm^{-1} (C=O stretching vibrations of peptide bonds), the amide II, 1500–1600 cm^{-1} (N–H bending/C–N stretching modes) and the amide III, 1200–1400 cm^{-1}, (N–H in-plane and C–N stretching vibrations) regions, all associated with the secondary structure conformational state of the proteins (Jackson & Mantsch, 1995), were among the most abundant peaks identified in the FTIR spectra. Comparing the FTIR spectra of the cryogels and the individual protein and sugar constituents (data not shown), it was confirmed that the presence of glucose and trehalose does not modify the aspects of the amide I band, which is in agreement with the findings of Belton and Gil (1994). By deconvoluting the amide I band, four different secondary structure conformations assigned to aggregated β-sheet (1691–1980 cm^{-1}), β-turn (1677–1670 cm^{-1}), α-helix (1655–1651 cm^{-1}) and β-sheet (1630–1623 cm^{-1}) were identified (Fig. 8B) (Daniloski et al., 2022). As for single protein cryogels, the NaCN exemplars were primarily composed of α-helices (60% α-helix, 31% β-sheet), whilst in the case of WPI the β-sheets were predominant (65% β-sheet, 23% α-helix; Fig. 8B). Our findings are in line with the observations of Hussain et al. (2012), who reported that the heat treatment of WPI promotes the establishment of β-sheets at the cost of α-helix and β-turn secondary structures. On the other hand, caseins are known as lacking or having little secondary structure conformation including α-helix, β-sheet, β-turns and 20–25% polyproline II (Markoska et al., 2020). Nonetheless, processing parameters such as heating, cooling and acidification may result in significant changes in the structure conformation of caseins. In a recent study, Markoska et al. (2021) demonstrated that the acidification of β-casein dispersions was accompanied by an abrupt increase in the amount of α-helices at the expense of random coils. It is therefore assumed that the predominance of the α-helix in the NaCN cryogels may stem from changes in the casein structure during the fermentation process. However, the hypothesis needs to be cross validated using additional analytical techniques. In the case of the mixed protein-based cryogels, the predominance of the α-helix and β-sheets was modified proportionally to the $m_{NaCN/WPI}$ (Fig. 7B). Nevertheless, no clear tendency was observed concerning the amount of β-turns and aggregated β-sheets. Finally, it should be noted that distinctive glucose and trehalose peaks were identified in all cryogels at 1149, 1107, 1078, 1034 and 989 cm^{-1} (Kačuráková et al., 2000; Márquez et al., 2018) and therefore, only a small amount of the sugars were utilised by LGG for its metabolic activity.

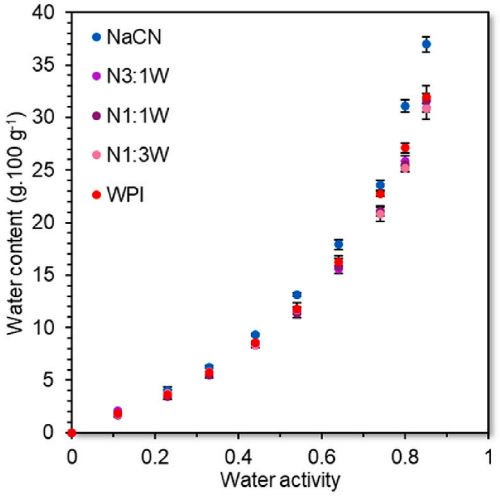

Fig. 8. Water mass fraction changes of cryogels as influenced by increasing water activity monitored by dynamic vapour sorption.

3.2.3. Water vapour sorption isotherms

On the completion of the freeze-drying process, the water content of the cryogels ranged from 4.0 to 4.6 g H_2O.100 g^{-1} (Table 1). The water vapour sorption isotherms of the cryogels obtained from DVS analysis are illustrated in Fig. 8. According to the Brunauer classification, the sorption isotherms obtained from the cryogels were associated to type III

Table 1
Milk protein cryogels moisture and calculated GAB equation parameters fitted with water vapour adsorption data.

	Moisture ($g.100g^{-1}$)	X_m ($g.100g^{-1}$)	C (−)	k (−)	S_m ($m^2.g^{-1}$)
NaCN	4.5 ± 0.5^{a}	11.53 ± 0.12^{a}	1.99 ± 0.03^{c}	0.61 ± 0.03^{a}	403.4 ± 4.1^{a}
N3:1W	4.1 ± 0.6^{a}	12.29 ± 0.11^{ab}	1.78 ± 0.01^{b}	0.56 ± 0.00^{a}	430.0 ± 4.0^{ab}
N1:1W	4.0 ± 0.5^{a}	12.61 ± 0.04^{ab}	1.73 ± 0.01^{ab}	0.54 ± 0.01^{a}	441.5 ± 1.4^{ab}
N1:3W	4.2 ± 0.7^{a}	13.00 ± 0.66^{bc}	1.71 ± 0.01^{a}	0.54 ± 0.03^{a}	455.0 ± 23.3^{bc}
WPI	4.6 ± 0.5^{a}	13.95 ± 0.10^{c}	1.70 ± 0.01^{a}	0.54 ± 0.00^{a}	488.2 ± 3.5^{c}

Abbreviations used: X_m: moisture content at monolayer completion, C: a constant that depicts the free enthalpy energy difference between the monolayer and pure liquid water molecules, k: a constant correcting the properties of the multilayer molecules and S_m: the surface of the monolayer. $^{a\text{-}c}$Different letters between the cryogels denote a significant difference ($p < 0.05$) according to Tukey's post hoc means comparison test.

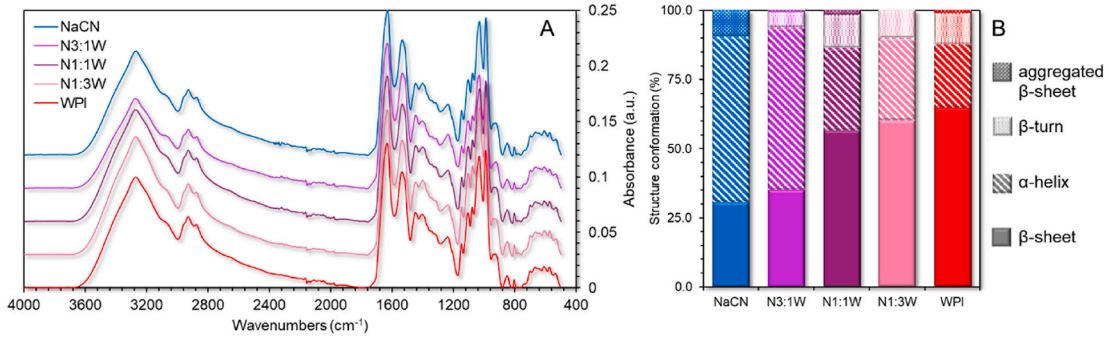

Fig. 7. Fourier transform infrared spectroscopy spectra of the cryogels of NaCN, WPI and their blends (A) and the average protein secondary structure conformation distribution obtained from amide I peak deconvolution (B, n = 2).

i.e., Flory-Huggins, which are characteristic of food matrices rich in soluble components such as sugars and polyols (Rao et al., 2014). Similar water vapour sorption isotherm patterns have also been reported in whey protein-based cryogels and aerogels (Manzocco et al., 2022). At low a_w values ($a_w < 0.23$), no significant differences were found in the moisture content of the cryogels. The progressive increase in the relative water vapour pressure amplified the moisture content discrepancies among the systems. To understand the impact of the $m_{NaCN/WPI}$ on the water vapour adsorption dynamics, the moisture − a_w data was satisfactorily fitted ($R^2 > 0.99$) into the GAB model (Eq. (1)). As shown in Table 1, the monolayer water content (X_m) exhibited an increase proportional to the $m_{NaCN/WPI}$ increase, which is associated with highly structured water molecules chemisorbed via hydrogen bond interactions to the binding polar groups ($-COO^-$, $-NH^+$, $-OH$) of proteins (Kinsella et al., 1986). It is well established that the monolayer water content of proteins may range from 2 to 10 g.100 g^{-1}, with caseins exhibiting a lower water vapour adsorbing ability ($X_m \sim 5.5$) than β-lactoglobulin ($X_m \sim 6.67$) (Kinsella et al., 1986). The discrepancies in the X_m values of the cryogels can be generally ascribed to their high mass fraction in highly hygroscopic constituents such as trehalose, glucose and glycerol, with the latter having a dominant effect (Farahnaky et al., 2009). It should also be noted that the changes in the structure conformational state induced by the treatments (i.e. pasteurisation and acidification) of the wet protein precursor may also affect (to a lesser extent) the water molecule adsorption, as additional binding sites are exposed. As displayed in the PCA biplot (Suppl. Fig. 4), the X_m was closely associated with the secondary structure conformation of the proteins (i.e., the prevalence of α-helix and β-sheet) and $T_{g,1}$. Interestingly, no specific dependence of X_m on the porosity and bulk density was found, which can be attributed to the inadequacy of the X-ray microtomography to provide an accurate estimation of the microporosity, as BET analysis could not be implemented for the determination of the specific surface area.

Similarly to X_m values, the calculated surface area (S_m) was increased reciprocally to the $m_{NaCN/WPI}$ (Table 1). S_m is considered a measure of the number of water molecules binding sites (protein polar groups) and therefore, the extent of hydration at a specific relative water vapour pressure (Kinsella et al., 1986). For milk protein powders, S_m ranges from ca. 140–256 $m^2\ g^{-1}$, whilst significantly higher values have been reported in agglomerated or aggregated milk protein fractals, such as cheese curds (800–1200 $m^2\ g^{-1}$). It is therefore assumed that the LGG-induced fermentation of the milk-based wet precursor had a contributory role to the increase of the surface area of the cryogels i.e., 403−488 $m^2\ g^{-1}$ (Table 1).

3.2.4. Thermal properties

For an overview of the thermal stability of the milk protein-based cryogels, the TGA thermographs of the individual ingredients (Fig. 9A) and the cryogels obtained shortly after the completion of the freeze-drying process (Fig. 9B) were acquired. As seen in Fig. 9A, milk proteins experienced two major weight loss events: firstly, an approx. 7.5% mass loss in the range of 30–110 °C ($T_{1,mid} = 45$ °C), which is ascribed to unbound water evaporation (Talón et al., 2019), and secondly, a 55−62% loss of the initial mass in the range of 250–400 °C ($T_{2,onset} = 257$ °C and $T_{2,mid} = 286$ °C), which is indicative of the concomitant thermal decomposition of the protein and residual milkfat matter (Koupantsis et al., 2016; Talón et al., 2019). Moreover, a minor weight loss event at ca. 162 °C was recorded in the TGA spectra of WPI, which is most probably associated with the presence of residual monohydrate lactose, i.e., water of crystallisation loss (Listiohadi et al., 2009). As for sugars, trehalose underwent a low temperature weight loss (about 6% of the initial mass) at 30−110 °C, associated with the water evaporation. Both sugars underwent thermal decomposition at T_{onset} above 200 °C, whilst glycerol experienced an abrupt weight loss at $T_{onset} = 187$ °C, which is in agreement with the literature data (Talón et al., 2019).

Concerning the TGA spectra of the cryogels, three major weight loss events were recorded (Fig. 9B). In accordance with the individual milk proteins, a mass loss (approx. 4.5%) was detected at $T_{1,mid} = 50$ °C associated with the evaporation of the unbound water (Table 2). The intermediate temperature ($T_{2,mid} = 186$ °C) mass loss event was most probably related to the thermal decomposition of glycerol, and the glycation of the protein molecules i.e., non-enzymatic browning, among others. In the latter case, the weight losses mainly refer to the release of water (Schiff base reaction – early glycation stage) and the volatile products of the Amadori rearrangement and Strecker reactions (van Boekel, 2006). Finally, the thermal decomposition of the cryogels took place at $T_{3,onset} = 301$ °C. For all the tested cryogel systems, no significant ($p > 0.05$) shift in the onset and midpoints of the TGA steps was observed, which is attributed to their compositional similarities and the minor differences in the thermal stability of the individual milk proteins.

As a successive analytical step, the physical state of the cryogels was measured by means of DSC and TMA. According to the DSC

Table 2
Thermophysical properties of the cryogels.

	DSC T_g (°C)	TMA $T_{g,1}$ (°C)	TMA $T_{g,2}$ (°C)
NaCN	99.3	33.4	112.0
N3:1W	98.9	Nd	105.5
N1:1W	98.7	38.1	112.8
N1:3W	99.2	41.2	101.3
WPI	99.3	45.7	110.9

TMA T_g of individual components (°C): NaCN = 47.6, WPI = 52.4, trehalose = 125.6, glucose 55.0. Nd = not detected.

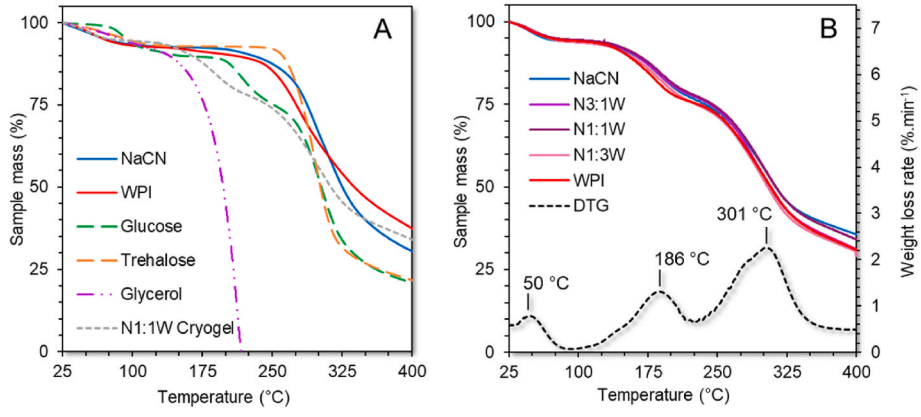

Fig. 9. TGA thermographs of the individual components of the cryogels (A) and TGA (continuous lines) and DTG (dashed line) of the cryogels (B) measured at 5 °C min^{-1}.

thermographs (data not shown), a transition from the glassy to the rubbery state was identified in the 98–100 °C temperature region, which is in keeping with the findings of (Manzocco et al., 2022) on WPI-based aerogels and cryogels. Nonetheless, the differences in the calculated $T_{g,mid}$ values among the cryogel samples were not significant (Table 2). To obtain a more accurate overview of their thermophysical contributory role, the components of the cryogels were individually analysed by TMA (Fig. 10A). As seen in Table 2, NaCN and WPI protein precursors underwent glass transition at 47.6 and 52.4 °C, respectively. This is in close agreement with the observations of Adhikari et al. (2009) and Boonyai et al. (2006). As for sugars, amorphous (freeze-dried) trehalose and glucose underwent glass transition at 125.6 and 55.0 °C, respectively. The TMA spectra of the cryogels (Fig. 10B, Table 2), evidenced the presence of two glass transition regions: $T_{g,1}$ = 33−46 °C and $T_{g,2}$ = 101−126 °C, depending on the $m_{NaCN/WPI}$. Except for the N3:1W system, the $T_{g,1}$ values decreased proportionally to the $m_{NaCN/WPI}$ ($T_{g,1} = -11.9\ m_{NaCN/WPI} + 44.8$, $R^2 = 0.975$). This finding implies that the $T_{g,1}$ denotes the temperature region where the softening of the cryogels occurs as a result of the non-covalent interchain protein interactions (e.g., hydrogen bonding and hydrophobic interactions) weakening. A good correlation was found between the prevalence of the β-sheet or α-helix structure conformational state of the proteins and the $T_{g,1}$ of the cryogels ($r = 0.910$, $p < 0.05$ for β-sheet, and $r = -0.860$, $p < 0.01$ for α-helix), which demonstrates that the glass transition at $T_{g,1}$ is closely associated with the unfolding ability of the proteins upon mechanical compression. Confirming our assumption, DeBenedictis and Keten (2019) reported that the dissipated energy, normalised to the protein characteristics, was significantly higher in β-sheet than in α-helix protein motifs. This was attributed primarily to the ability of the hydrogen bond network of the β-sheet strands to be mechanically loaded in a collective mode that requires larger forces to rupture. Notably, once the required energy for weakening the protein interchain molecular interactions was dissipated, both the WPI powder and its cryogel exemplars exhibited the lowest deformability upon compression (Fig. 10B), which may be indicative of their brittle and friable character (Lefèvre et al., 2005).

Contrary to $T_{g,1}$, the $T_{g,2}$ values did not show any clear dependence on the $m_{NaCN/WPI}$, suggesting that the $T_{g,2}$ is not associated with changes in the interchain protein interactions. Instead, the $T_{g,2}$ of the cryogels were quite close to those recorded for the amorphous sugars i.e., trehalose ($T_g \sim 125$ °C) and glucose ($T_g \sim 55$ °C), and thus, it is assumed that the $T_{g,2}$ depicts the temperature region in which the sugar blend stiffness is being dropped. At $T > T_{g,2}$, a substantial decrease in the deformability of the cryogels was observed, indicating their structural collapse.

3.2.5. Mechanical properties

The mechanical characteristics of the cryogel monoliths were probed by indentation testing (Table 3). In general, the hardness (i.e., maximum force at rupture) and stiffness of the cryogels were governed by the thickness and uniformity of the protein filamentous cryogel construct (Fig. 6C). In most cases, aerogels and cryogels are characterised as brittle and plastic materials.

In relation to the obtained force – indentation curve profiles (for an example see Suppl. Fig. 1), all protein cryogels exhibited a predominantly brittle character, which was in the agreement with the findings of Chen et al. (2013). Significant differences were detected in the hardness, stiffness and energy dissipated for the cryogel rupture. Nonetheless, it was not possible to identify any proportionality between the mechanical properties and the $m_{NaCN/WPI}$. On the other hand, the energy dissipated (work) for the structural collapse of the cryogels exhibited significant ($p < 0.05$) correlations with the TMA determined $T_{g,1}$ ($r = -0.68$), the protein structure conformational state i.e., α-helix ($r = 0.85$) and β-sheet ($r = -0.81$) prevalence, and $m_{NaCN/WPI}$ ($r = 0.65$). Nonetheless, it was not possible to find a common mechanistic conjecture regarding the impact of the structure conformational state of the proteins and the mechanical energy, as in the case of the TMA results. This may be attributed to the fact that the work required for the structural collapse of the cryogels is macroscopically driven e.g., creation and propagation of structure imperfections due to the indentation forces. Finally, it should be noted that a good correlation between work and stiffness ($r = -0.55$, $p < 0.05$) was found, which signifies that the lowest amount of energy is dissipated in the most brittle cryogel constructs.

3.2.6. Water reconstitution behaviour

To understand to the reconstitution behaviour of the cryogel monoliths once they come into contact with water, a real-time particle mean size assessment method was implemented (Fig. 11, Table 4). In a mechanistic context, the disintegration of dry particulate-based formulations e.g., spray dried powders and lyophilizates, tablets, aerogels etc. can be described by four kinetically driven physical phenomena including wetting, swelling, dispersion and dissolution (Forny et al.,

Table 3
Mechanical properties of the cryogels under penetration stress.

	Hardness (N)	Stiffness ($N.mm^{-1}$)	Work (mJ)
NaCN	15.8 ± 5.5^{ab}	12.2 ± 3.0^{ab}	9.9 ± 3.9^{a}
N3:1W	15.1 ± 1.9^{ab}	6.8 ± 1.3^{a}	17.3 ± 5.6^{b}
N1:1W	12.9 ± 1.4^{a}	16.9 ± 2.9^{b}	4.9 ± 2.4^{a}
N1:3W	19.9 ± 4.2^{b}	30.8 ± 6.5^{c}	6.1 ± 1.8^{a}
WPI	10.4 ± 1.1^{a}	11.4 ± 2.2^{ab}	4.6 ± 1.3^{a}

[a-c]Different letters between the cryogels denote a significant difference ($p < 0.05$) according to Tukey's post hoc means comparison test.

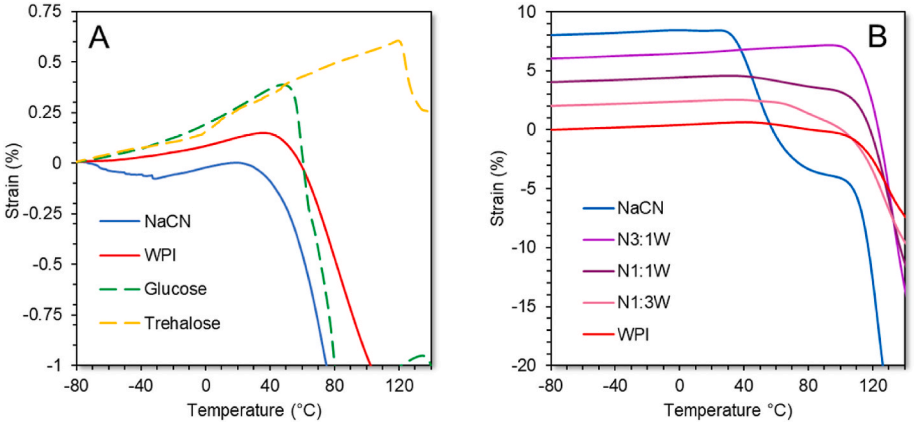

Fig. 10. Thermo-mechanical profile of individual ingredients of the cryogels (A) and milk protein cryogels (B). For improved readability, the TMA spectra of NaCN, N3:1W, N1:1W and N1:3W cryogels were shifted upward by 8, 6, 4 and 2%, respectively.

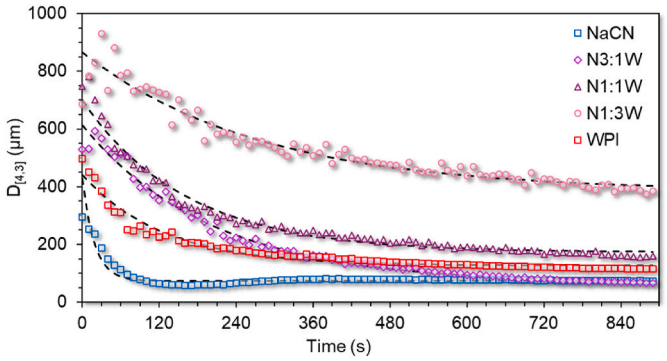

Fig. 11. Disintegration profile of the NaCN, WPI and blend cryogels measured at 20 °C and with a constant shear speed of 3500 rpm. Black lines represent the fitted data using the first-order exponential decay model (Eq. (4)). The curves and the points represents the average of 5 individual disintegration experiments.

Table 4
Disintegration parameters of the cryogels.

	$D_{[4,3]\ t0}$ (μm)	$D_{[4,3]\ t\infty}$ (μm)	$\tau_{1/2}$ (s)	$\tau_{99\%}$ (s)
NaCN	407.2 ± 23.7^{a}	75.8 ± 1.8^{a}	14.2 ± 1.0^{a}	94.2 ± 6.5^{a}
N3:1W	632.9 ± 29.5^{b}	68.0 ± 15.0^{a}	131.9 ± 11.0^{cd}	876.1 ± 73.2^{c}
N1:1W	685.7 ± 174.3^{c}	126.1 ± 19.2^{b}	100.0 ± 1.3^{bc}	706.2 ± 65.3^{bc}
N1:3W	956.3 ± 71.9^{d}	406.8 ± 96.9^{c}	130.3 ± 33.3^{d}	865.9 ± 221.0^{c}
WPI	449.9 ± 83.5^{a}	126.6 ± 35.7^{ab}	84.8 ± 10.7^{b}	563.1 ± 65.8^{d}

Abbreviation used: $D_{[4,3]\ t0}$: particle size (in μm) at t = 0 min; $D_{[4,3]\ t\infty}$: particle size (in μm) at t = ∞ min; $\tau_{1/2}$: time (in seconds) required to obtain a 50% particle size reduction; $\tau_{99\%}$: time (in second) required to obtain a 99% particle size reduction. $^{a\text{-}d}$Different letters between the cryogels denote a significant difference ($p < 0.05$) according to Tukey's post hoc means comparison test (n = 5).

2011; Markl & Zeitler, 2017). As illustrated in Fig. 11, the immersion of the cryogel monoliths into the water tank resulted in their rapid disintegration into large agglomerates ranging from $D_{[4,3]\ t0} = 407–956$ μm in size. In the early stages of the disintegration process, the wetting of the outer matrix surface and the progressive capillary diffusion of water are known to result into the omni-directional enlargement of the particles, leading to an increase in internal pressure and pushing apart the adjoining agglomerates (Markl & Zeitler, 2017). Indeed, as displayed in the PCA biplot (Suppl. Fig. 4), the $D_{[4,3]\ t0}$ values were correlated negatively with the porosity (φ) of the cryogels and positively with their bulk density and shrinkage. Therefore, due to their more porous and compact microstructure, the mixed protein-based cryogels tended to break down into the larger agglomerates more than their individual protein exemplars. As the reconstitution process progresses, the loose particles start to reduce in size, which is the result of fast-pacing mass transfer phenomena occurring at the solid – solvent interface (Forny et al., 2011). The agglomerate dissolution half-time ($\tau_{½}$), $\tau_{99\%}$ and the residual (non-dissolved) cryogel particles $D_{[4,3]\ t\infty}$ were significantly higher ($p < 0.05$) in the case of the mixed protein cryogels (Table 4). A significant correlation ($r > 0.7$, $p < 0.05$) was identified between the dissolution parameters ($\tau_{½}$, $\tau_{99\%}$ and $D_{[4,3]\ t\infty}$) and the porosity, filamentous uniformity (span) hardness and stiffness of the cryogels (Suppl. Fig. 4), supporting the diffusion-driven mechanism of the cryogels dissolution behaviour.

4. Conclusions

A novel xero-scaffold was successfully developed based on freeze drying induced cryogels that deployed a pre-fermented milk protein-based hydrogel for embedding living probiotic bacteria cells i.e., *Lacticaseibacillus rhamnosus* GG. The microscopic assessment of the wall material of the cryogels evidenced the satisfactory intrenching of the LGG bacterial cells, an effect that was independent of their compositional profile. The volume contraction and the microstructural conformation of the cryogels were inextricably associated with the behaviour of acid hydrogel precursors during the fermentation step. The mixed protein-based cryogels underwent a higher degree of volume contraction during freeze-drying, resulting in a more compacted, hard and stiff, yet less water-reconstitutable, construct than their individual protein exemplars. From a microstructural viewpoint, the cryogels exhibited a sponge-like microstructure in terms of the macropore volume fraction, as well as the thickness and uniformity of the protein network ligaments, notably dependent on the protein composition of their wet hydrogel precursors. A coarse lamellate wall matter microstructure was observed in the NaCN-rich cryogels as opposed to their WPI-rich exemplars that exerted a compact globular aggregated conformation. The water vapour sorption and the thermo-mechanical properties of the cryogels were the only characteristics showing a consistent dependence on the $m_{NaCN/WPI}$. The second part of this study will assess the feasibility of the cryogels hereby developed to preserve the biological activity of the LGG cells and will report on the inactivation kinetics of LGG under controlled storage conditions, its release and survival throughout in vitro digestion, and the peptidomic profile of the gastric and intestinal digesta as influenced by the protein composition and the physicochemical, microstructural and thermo-mechanical properties of the cryogels disclosed in this work.

Credit author statement

Thierry Hellebois: Conceptualisation, Investigation, Formal analysis, Writing Original Draft: Writing-Review-Editing.

Romain Canuel: Investigation, Formal analysis, Writing-Review-Editing.

Frédéric Addiego: Investigation, Formal analysis, Writing-Review-Editing.

Jean-Nicolas Audinot: Investigation, Formal analysis, Writing-Review-Editing.

Claire Gaiani: Conceptualisation, Writing-Review-Editing, Supervision (TH).

Alexander Shaplov: Investigation, Formal analysis, Writing-Review-Editing.

Christos Soukoulis: Conceptualisation, Writing-Review-Editing, Supervision (TH), Project administration, Funding acquisition.

Declaration of competing interest

The authors declare that they have no known competing financial interests or personal relationships that could have appeared to influence the work reported in this paper.

Data availability

Data will be made available on request.

Acknowledgements

This work was supported by the Fonds National de la Recherche Luxembourg (Project PROCEED: CORE/2018/SR/12675439). The authors would like to acknowledge Manon Hiolle (Ingredia, Arras, France) for providing the WPI. Carole Jeandel and Carole Perroud are acknowledged for their technical support with DSC and DVS analyses.

Appendix A. Supplementary data

Supplementary data to this article can be found online at https://doi.org/10.1016/j.foodhyd.2023.108641.

References

Adhikari, B., Howes, T., Bhandari, B. R., & Langrish, T. A. G. (2009). Effect of addition of proteins on the production of amorphous sucrose powder through spray drying. *Journal of Food Engineering, 94*(2), 144–153. https://doi.org/10.1016/j.jfoodeng.2009.01.029

Ahmadi, M., Madadlou, A., & Saboury, A. A. (2016). Whey protein aerogel as blended with cellulose crystalline particles or loaded with fish oil. *Food Chemistry, 196*, 1016–1022. https://doi.org/10.1016/j.foodchem.2015.10.031

Aschenbrenner, M., Först, P., & Kulozik, U. (2015). *Freeze-drying of probiotics* (pp. 213–241). https://doi.org/10.1201/b18807-15

Bektas, E. I., Gurel Pekozer, G., Kök, F. N., & Torun Kose, G. (2021). Evaluation of natural gum-based cryogels for soft tissue engineering. *Carbohydrate Polymers, 271*, Article 118407. https://doi.org/10.1016/j.carbpol.2021.118407

Belton, P. S., & Gil, A. M. (1994). IR and Raman spectroscopic studies of the interaction of trehalose with hen egg white lysozyme. *Biopolymers, 34*(7), 957–961. https://doi.org/10.1002/bip.360340713

van den Berg, C., & Bruin, S. (1981). Water activity and its estimation in food systems: Theoretical aspects. In L. B. Rockland, & G. F. Stewart (Eds.), *Water activity: Influences on food quality* (pp. 1–61). Academic Press. https://doi.org/10.1016/B978-0-12-591350-8.50007-3.

Betz, M., García-González, C. A., Subrahmanyam, R. P., Smirnova, I., & Kulozik, U. (2012). Preparation of novel whey protein-based aerogels as drug carriers for life science applications. *The Journal of Supercritical Fluids, 72*, 111–119. https://doi.org/10.1016/j.supflu.2012.08.019

van Boekel, M. A. J. S. (2006). Formation of flavour compounds in the Maillard reaction. *Biotechnology Advances, 24*(2), 230–233. https://doi.org/10.1016/j.biotechadv.2005.11.004

Boonyai, P., Bhandari, B., & Howes, T. (2006). Applications of thermal mechanical compression tests in food powder analysis. *International Journal of Food Properties, 9*(1), 127–134. https://doi.org/10.1080/10942910500473988

Burgain, J., Corgneau, M., Scher, J., & Gaiani, C. (2015). Chapter 20 - encapsulation of probiotics in milk protein microcapsules. In L. M. C. Sagis (Ed.), *Microencapsulation and microspheres for food applications* (pp. 391–406). Academic Press. http://www.sciencedirect.com/science/article/pii/B9780128003503000194.

Capozzi, V., Arena, M. P., Russo, P., Spano, G., & Fiocco, D. (2016). Chapter 16 - stressors and food environment: Toward strategies to improve robustness and stress tolerance in probiotics. In R. R. Watson, & V. R. Preedy (Eds.), *Probiotics, prebiotics, and synbiotics* (pp. 245–256). Academic Press. http://www.sciencedirect.com/science/article/pii/B9780128021897000162.

Chen, H.-B., Wang, Y.-Z., & Schiraldi, D. A. (2013). Foam-like materials based on whey protein isolate. *European Polymer Journal, 49*(10), 3387–3391. https://doi.org/10.1016/j.eurpolymj.2013.07.019

Daniloski, D., McCarthy, N. A., Markoska, T., Auldist, M. J., & Vasiljevic, T. (2022). Conformational and physicochemical characteristics of bovine skim milk obtained from cows with different genetic variants of β-casein. *Food Hydrocolloids, 124*, Article 107186. https://doi.org/10.1016/j.foodhyd.2021.107186

DeBenedictis, E. P., & Keten, S. (2019). Mechanical unfolding of alpha- and beta-helical protein motifs. *Soft Matter, 15*(6), 1243–1252. https://doi.org/10.1039/C8SM02046A

Donato, L., Kolodziejcyk, E., & Rouvet, M. (2011). Mixtures of whey protein microgels and soluble aggregates as building blocks to control rheology and structure of acid induced cold-set gels. *Food Hydrocolloids, 25*(4), 734–742. https://doi.org/10.1016/j.foodhyd.2010.08.020

Farahnaky, A., Ansari, S., & Majzoobi, M. (2009). Effect of glycerol on the moisture sorption isotherms of figs. *Journal of Food Engineering, 93*(4), 468–473. https://doi.org/10.1016/j.jfoodeng.2009.02.014

Fontes-Candia, C., Jiménez-Barrios, P., Miralles, B., Recio, I., López-Rubio, A., & Martínez-Sanz, M. (2022). Development of polysaccharide-casein gel-like structures resistant to in vitro gastric digestion. *Food Hydrocolloids, 127*, Article 107505. https://doi.org/10.1016/j.foodhyd.2022.107505

Forny, L., Marabi, A., & Palzer, S. (2011). Wetting, disintegration and dissolution of agglomerated water soluble powders. *Powder Technology, 206*(1), 72–78. https://doi.org/10.1016/j.powtec.2010.07.022

Gomand, F., Borges, F., Guerin, J., El-Kirat-Chatel, S., Francius, G., Dumas, D., Burgain, J., & Gaiani, C. (2019). Adhesive interactions between lactic acid bacteria and β-lactoglobulin: Specificity and impact on bacterial location in whey protein isolate. *Frontiers in Microbiology, 10*. https://doi.org/10.3389/fmicb.2019.01512

Groult, S., Buwalda, S., & Budtova, T. (2021). Pectin hydrogels, aerogels, cryogels and xerogels: Influence of drying on structural and release properties. *European Polymer Journal, 149*, Article 110386. https://doi.org/10.1016/j.eurpolymj.2021.110386

Gun'ko, V. M., Savina, I. N., & Mikhalovsky, S. V. (2013). Cryogels: Morphological, structural and adsorption characterisation. *Advances in Colloid and Interface Science, 187*, 1–46. https://doi.org/10.1016/j.cis.2012.11.001. –*188*.

Gu, Q., Yin, Y., Yan, X., Liu, X., Liu, F., & McClements, D. J. (2022). Encapsulation of multiple probiotics, synbiotics, or nutrabiotics for improved health effects: A review. *Advances in Colloid and Interface Science, 309*, Article 102781. https://doi.org/10.1016/j.cis.2022.102781

Heidebach, T., Först, P., & Kulozik, U. (2009). Transglutaminase-induced caseinate gelation for the microencapsulation of probiotic cells. *International Dairy Journal, 19*(2), 77–84. https://doi.org/10.1016/j.idairyj.2008.08.003

Hellebois, T., Gaiani, C., Cambier, S., Noo, A., & Soukoulis, C. (2022). Exploration of the co-structuring and stabilising role of flaxseed gum in whey protein isolate based cryo-hydrogels. *Carbohydrate Polymers, 289*, Article 119424. https://doi.org/10.1016/j.carbpol.2022.119424

Hellebois, T., Gaiani, C., & Soukoulis, C. (2022). Freeze − thaw induced structuration of whey protein − alfalfa (Medicago sativa L.) galactomannan binary systems. *Food Hydrocolloids, 125*, Article 107389. https://doi.org/10.1016/j.foodhyd.2021.107389

Hill, C., Guarner, F., Reid, G., Gibson, G. R., Merenstein, D. J., Pot, B., Morelli, L., Canani, R. B., Flint, H. J., Salminen, S., Calder, P. C., & Sanders, M. E. (2014). The International Scientific Association for Probiotics and Prebiotics consensus statement on the scope and appropriate use of the term probiotic. *Nature Reviews Gastroenterology & Hepatology, 11*(8), 506–514. https://doi.org/10.1038/nrgastro.2014.66

Hussain, R., Gaiani, C., Jeandel, C., Ghanbaja, J., & Scher, J. (2012). Combined effect of heat treatment and ionic strength on the functionality of whey proteins. *Journal of Dairy Science, 95*(11), 6260–6273. https://doi.org/10.3168/jds.2012-5416

Jackson, M., & Mantsch, H. H. (1995). The use and misuse of FTIR spectroscopy in the determination of protein structure. *Critical Reviews in Biochemistry and Molecular Biology, 30*(2), 95–120. https://doi.org/10.3109/10409239509085140

Jiang, Z., Li, M., McClements, D. J., Liu, X., & Liu, F. (2022). Recent advances in the design and fabrication of probiotic delivery systems to target intestinal inflammation. *Food Hydrocolloids, 125*, Article 107438. https://doi.org/10.1016/j.foodhyd.2021.107438

Kačuráková, M., Capek, P., Sasinková, V., Wellner, N., & Ebringerová, A. (2000). FT-IR study of plant cell wall model compounds: Pectic polysaccharides and hemicelluloses. *Carbohydrate Polymers, 43*(2), 195–203. https://doi.org/10.1016/S0144-8617(00)00151-X

Kiepś, J., & Dembczyński, R. (2022). Current trends in the production of probiotic formulations. *Foods, 11*(15), 2330. https://doi.org/10.3390/foods11152330

Kinsella, J. E., Fox, P. F., & Rockland, L. B. (1986). Water sorption by proteins: Milk and whey proteins. *CRC Critical Reviews in Food Science & Nutrition, 24*(2), 91–139. https://doi.org/10.1080/10408398609527434

Kleemann, C., Schuster, R., Rosenecker, E., Selmer, I., Smirnova, I., & Kulozik, U. (2020). In-vitro-digestion and swelling kinetics of whey protein, egg white protein and sodium caseinate aerogels. *Food Hydrocolloids, 101*, Article 105534. https://doi.org/10.1016/j.foodhyd.2019.105534

Kleemann, C., Selmer, I., Smirnova, I., & Kulozik, U. (2018). Tailor made protein based aerogel particles from egg white protein, whey protein isolate and sodium caseinate: Influence of the preceding hydrogel characteristics. *Food Hydrocolloids, 83*, 365–374. https://doi.org/10.1016/j.foodhyd.2018.05.021

Koh, W. Y., Lim, X. X., Tan, T.-C., Kobun, R., & Rasti, B. (2022). Encapsulated probiotics: Potential techniques and coating materials for non-dairy food applications. *Applied Sciences, 12*(19), Article 10005. https://doi.org/10.3390/app121910005

Koupantsis, T., Pavlidou, E., & Paraskevopoulou, A. (2016). Glycerol and tannic acid as applied in the preparation of milk proteins – CMC complex coavervates for flavour encapsulation. *Food Hydrocolloids, 57*, 62–71. https://doi.org/10.1016/j.foodhyd.2016.01.007

Lefèvre, T., Subirade, M., & Pézolet, M. (2005). Molecular description of the formation and structure of plasticized globular protein films. *Biomacromolecules, 6*(6), 3209–3219. https://doi.org/10.1021/bm050540u

Listiohadi, Y., Hourigan, J. A., Sleigh, R. W., & Steele, R. J. (2009). Thermal analysis of amorphous lactose and α-lactose monohydrate. *Dairy Science & Technology, 89*(1), 43–67. https://doi.org/10.1051/dst:2008027

Lozinsky, V. I. (2018). Cryostructuring of polymeric systems. 50.† cryogels and cryotropic gel-formation: Terms and definitions. *Gels, 4*(3), 77. https://doi.org/10.3390/gels4030077

Lozinsky, V. I. (2020). Cryostructuring of polymeric systems. 55. Retrospective view on the more than 40 Years of studies performed in the A.N.nesmeyanov institute of organoelement compounds with respect of the cryostructuring processes in polymeric systems. *Gels, 6*(3), 29. https://doi.org/10.3390/gels6030029

Lucey, J. A. (2002). Formation and physical properties of milk protein gels. *Journal of Dairy Science, 85*(2), 281–294. https://doi.org/10.3168/jds.S0022-0302(02)74078-2

Lucey, J. A. (2020). Chapter 16 - milk protein gels. In M. Boland, & H. Singh (Eds.), *Milk proteins* (3rd ed., pp. 599–632). Academic Press. https://doi.org/10.1016/B978-0-12-815251-5.00016-5.

Manzocco, L., Mikkonen, K. S., & García-González, C. A. (2021). Aerogels as porous structures for food applications: Smart ingredients and novel packaging materials. *Food Structure, 28*, Article 100188. https://doi.org/10.1016/j.foostr.2021.100188

Manzocco, L., Plazzotta, S., Powell, J., de Vries, A., Rousseau, D., & Calligaris, S. (2022). Structural characterisation and sorption capability of whey protein aerogels obtained by freeze-drying or supercritical drying. *Food Hydrocolloids, 122*, Article 107117. https://doi.org/10.1016/j.foodhyd.2021.107117

Markl, D., & Zeitler, J. A. (2017). A review of disintegration mechanisms and measurement techniques. *Pharmaceutical Research, 34*(5), 890–917. https://doi.org/10.1007/s11095-017-2129-z

Markoska, T., Daniloski, D., Vasiljevic, T., & Huppertz, T. (2021). Structural changes of β-casein induced by temperature and pH analysed by nuclear magnetic resonance, fourier-transform infrared spectroscopy, and chemometrics. *Molecules, 26*(24), 7650. https://doi.org/10.3390/molecules26247650

Markoska, T., Vasiljevic, T., & Huppertz, T. (2020). Unravelling conformational aspects of milk protein structure—contributions from nuclear magnetic resonance studies. *Foods, 9*(8), 1128. https://doi.org/10.3390/foods9081128

Márquez, M. J., Romani, D., Díaz, S. B., & Brandán, S. A. (2018). Structural and vibrational characterization of anhydrous and dihydrated species of trehalose based on the FTIR and FTRaman spectra and DFT calculations. *Journal of King Saud University Science, 30*(2), 229–249. https://doi.org/10.1016/j.jksus.2017.01.009

Mazza, G., & LeMaguer, M. (1978). Water sorption properties of yellow globe onion (Allium cepa L.). *Canadian Institute of Food Science and Technology Journal, 11*(4), 189–193. https://doi.org/10.1016/S0315-5463(78)73269-4

Nguyen, B. T., Nicolai, T., Chassenieux, C., Schmitt, C., & Bovetto, L. (2016). Heat-induced gelation of mixtures of whey protein isolate and sodium caseinate between pH 5.8 and pH 6.6. *Food Hydrocolloids, 61*, 433–441. https://doi.org/10.1016/j.foodhyd.2016.05.030

Pugnaloni, L. A., Matia-Merino, L., & Dickinson, E. (2005). Microstructure of acid-induced caseinate gels containing sucrose: Quantification from confocal microscopy and image analysis. *Colloids and Surfaces B: Biointerfaces, 42*(3–4), 211–217. https://doi.org/10.1016/j.colsurfb.2005.03.002

Quodbach, J., & Kleinebudde, P. (2014). A new apparatus for real-time assessment of the particle size distribution of disintegrating tablets. *Journal of Pharmaceutical Sciences, 103*(11), 3657–3665. https://doi.org/10.1002/jps.24168

Rao, M. A., Rizvi, S. S. H., Datta, A. K., & Ahmed, J. (2014). *Engineering properties of foods* (4th ed.). CRC Press.

Schorsch, C., Carrie, H., & Norton, I. T. (2000). Cross-linking casein micelles by a microbial transglutaminase: in#uence of cross-links in acid-induced gelation. *International Dairy Journal, 11*.

Selmer, I., Karnetzke, J., Kleemann, C., Lehtonen, M., Mikkonen, K. S., Kulozik, U., & Smirnova, I. (2019). Encapsulation of fish oil in protein aerogel micro-particles. *Journal of Food Engineering, 260*, 1–11. https://doi.org/10.1016/j.jfoodeng.2019.04.016

Selmer, I., Kleemann, C., Kulozik, U., Heinrich, S., & Smirnova, I. (2015). Development of egg white protein aerogels as new matrix material for microencapsulation in food. *The Journal of Supercritical Fluids, 106*, 42–49. https://doi.org/10.1016/j.supflu.2015.05.023

Shiekh, P. A., Andrabi, S. M., Singh, A., Majumder, S., & Kumar, A. (2021). Designing cryogels through cryostructuring of polymeric matrices for biomedical applications. *European Polymer Journal, 144*, Article 110234. https://doi.org/10.1016/j.eurpolymj.2020.110234

Soukoulis, C., Behboudi-Jobbehdar, S., Macnaughtan, W., Parmenter, C., & Fisk, I. D. (2017). Stability of Lactobacillus rhamnosus GG incorporated in edible films: Impact of anionic biopolymers and whey protein concentrate. *Food Hydrocolloids, 70*, 345–355. https://doi.org/10.1016/j.foodhyd.2017.04.014

Soukoulis, C., Cambier, S., Serchi, T., Tsevdou, M., Gaiani, C., Ferrer, P., Taoukis, P. S., & Hoffmann, L. (2019). Rheological and structural characterisation of whey protein acid gels co-structured with chia (Salvia hispanica L.) or flax seed (Linum usitatissimum L.) mucilage. *Food Hydrocolloids, 89*, 542–553. https://doi.org/10.1016/j.foodhyd.2018.11.002

Soukoulis, C., Panagiotidis, P., Koureli, R., & Tzia, C. (2007). Industrial yogurt manufacture: Monitoring of fermentation process and improvement of final product quality. *Journal of Dairy Science, 90*(6), 2641–2654. https://doi.org/10.3168/jds.2006-802

Soukoulis, C., Singh, P., Macnaughtan, W., Parmenter, C., & Fisk, I. D. (2016). Compositional and physicochemical factors governing the viability of Lactobacillus rhamnosus GG embedded in starch-protein based edible films. *Food Hydrocolloids, 52*, 876–887. https://doi.org/10.1016/j.foodhyd.2015.08.025

Talón, E., Lampi, A.-M., Vargas, M., Chiralt, A., Jouppila, K., & González-Martínez, C. (2019). Encapsulation of eugenol by spray-drying using whey protein isolate or lecithin: Release kinetics, antioxidant and antimicrobial properties. *Food Chemistry, 295*, 588–598. https://doi.org/10.1016/j.foodchem.2019.05.115

Volkova, N., & Berillo, D. (2021). Water uptake as a crucial factor on the properties of cryogels of gelatine cross-linked by dextran dialdehyde. *Gels, 7*(4), 159. https://doi.org/10.3390/gels7040159

Yao, M., Xie, J., Du, H., McClements, D. J., Xiao, H., & Li, L. (2020). Progress in microencapsulation of probiotics: A review. *Comprehensive Reviews in Food Science and Food Safety, 19*(2), 857–874. https://doi.org/10.1111/1541-4337.12532

Zou, F., & Budtova, T. (2021). Tailoring the morphology and properties of starch aerogels and cryogels via starch source and process parameter. *Carbohydrate Polymers, 255*, Article 117344. https://doi.org/10.1016/j.carbpol.2020.117344